A Candidate for the Least-massive Black Hole in the First 1.1 Billion Years of the Universe

(article starts on next page)

A Candidate for the Least-massive Black Hole in the First 1.1 Billion Years of the Universe

Masafusa Onoue[1,2,7] , Kohei Inayoshi[1] , Xuheng Ding[2] , Wenxiu Li[1] , Zhengrong Li[1] , Juan Molina[1,3] ,
Akio K. Inoue[4,5] , Linhua Jiang[1,6] , and Luis C. Ho[1,6]

[1] Kavli Institute for Astronomy and Astrophysics, Peking University, Beijing 100871, People's Republic of China; onoue@pku.edu.cn, inayoshi@pku.edu.cn
[2] Kavli Institute for the Physics and Mathematics of the Universe (Kavli IPMU, WPI), The University of Tokyo, Chiba 277-8583, Japan
[3] Department of Space, Earth and Environment, Chalmers University of Technology, Onsala Space Observatory, 439 92 Onsala, Sweden
[4] Waseda Research Institute for Science and Engineering, Faculty of Science and Engineering, Waseda University, 3-4-1, Okubo, Shinjuku, Tokyo 169-8555, Japan
[5] Department of Physics, School of Advanced Science and Engineering, Faculty of Science and Engineering, Waseda University, 3-4-1, Okubo, Shinjuku, Tokyo 169-8555, Japan
[6] Department of Astronomy, School of Physics, Peking University, Beijing 100871, People's Republic of China

Abstract

We report a candidate of a low-luminosity active galactic nucleus (AGN) at $z = 5$ that was selected from the first near-infrared images of the JWST CEERS project. This source, named CEERS-AGN-z5-1 at absolute 1450 Å magnitude $M_{1450} = -19.5 \pm 0.3$, was found via a visual selection of compact sources from a catalog of Lyman break galaxies at $z > 4$, taking advantage of the superb spatial resolution of the JWST/NIRCam images. The 20 photometric data available from CFHT, Hubble Space Telescope, Spitzer, and JWST suggest that the continuum shape of this source is reminiscent of that for an unobscured AGN, and there is a clear color excess in the filters where the redshifted Hβ+[O III] and Hα are covered. The estimated line luminosity is $L_{\mathrm{H}\beta+[\mathrm{O\,III}]} = 10^{43.0}$ erg s^{-1} and $L_{\mathrm{H}\alpha} = 10^{42.9}$ erg s^{-1} with the corresponding rest-frame equivalent width $\mathrm{EW}_{\mathrm{H}\beta+[\mathrm{O\,III}]} = 1100$ Å and $\mathrm{EW}_{\mathrm{H}\alpha} = 1600$ Å, respectively. Our spectral energy distribution fitting analysis favors the scenario that this object is either a strong broad-line emitter or even a super-Eddington accreting black hole (BH), although a possibility of an extremely young galaxy with moderate dust attenuation is not completely ruled out. The bolometric luminosity, $L_{\mathrm{bol}} = 2.5 \pm 0.3 \times 10^{44}$ erg s^{-1}, is consistent with those of $z < 0.35$ broad-line AGNs with $M_{\mathrm{BH}} \sim 10^6$ $M_\odot$ accreting at the Eddington limit. This new AGN population in the first 1.1 billion years of the universe may close the gap between the observed BH mass range at high redshift and that of BH seeds. Spectroscopic confirmation is awaited to secure the redshift and its AGN nature.

1. Introduction

The past two decades were a golden era of high-redshift quasar observations. Starting from the Sloan Digital Sky Survey (Fan et al. 2001a; Jiang et al. 2016), $\gtrsim 1000$ deg^2-class wide-field surveys have identified several hundred quasars in the epoch of cosmic reionization with the current redshift record of $z \sim 7.6$ (Banados et al. 2018; Wang et al. 2021; Yang et al. 2021). Follow-up spectroscopic studies have revealed that those quasars are powered by accreting massive BHs with masses greater than $M_{\mathrm{BH}} = 10^9 M_\odot$, despite their young ages (e.g., Wu et al. 2015; Shen et al. 2019). The formation and early growth history of massive BHs is one of the biggest mysteries of modern astronomy.

Exploring the origin of the massive BHs is still challenging because the brightest quasar population is already matured after experiencing rapid accretion episodes and losing the information on their seeding process. Currently, the least-massive BHs that have been spectroscopically confirmed at $z \gtrsim 5$ are those with $M_{\mathrm{BH}} \sim 10^8 M_\odot$ (e.g., Willott et al. 2010; Onoue et al. 2019), several orders of magnitudes heavier than the predicted seed mass

range ($10^{2-6} M_\odot$; see Inayoshi et al. 2020 for a recent review). Therefore, it is crucial to close the gap between the two mass regimes via detecting lower-mass BHs in epochs as early as possible.

Extensive efforts have been made with the Hubble Space Telescope (HST) to identify $z \gtrsim 6$ AGNs at the very faint end of the quasar/AGN luminosity function (UV magnitude -22 or fainter). No AGNs have been confirmed yet (Morishita et al. 2020; Fujimoto et al. 2022; Jiang et al. 2022), but with a few candidates at $z = 7$–8 (Ishikawa et al. 2022). A naive interpretation of their low success rates is that their point-source selection is not an effective approach to search for low-luminosity AGNs, because host-galaxy contamination becomes more severe (Bowler et al. 2021; Adams et al. 2022). On the other hand, a fraction of high-redshift quasars seem to have compact (<1 kpc) host galaxies, according to recent Atacama Large Millimeter/submillimeter Array observations of luminous $z > 6$ quasars (Neeleman et al. 2021; Walter et al. 2022).

Aside from pure AGN surveys, one possible alternative approach to find low-luminosity AGNs is to use samples of UV-selected galaxies. At redshift $4 < z < 6$, the UV luminosity functions of AGNs and Lyman break galaxies (LBGs) intersect with each other at $M_{\mathrm{UV}} \sim -23$ mag (Matsuoka et al. 2018; Ono et al. 2018; Stevans et al. 2018; Adams et al. 2022; Harikane et al. 2022a; Finkelstein & Bagley 2022; Li et al. 2022). Spectroscopic follow-up studies of $z \gtrsim 4$ LBGs have recently found several

---

candidates of AGNs and galaxy+AGN composite sources at the galaxy-dominated regime, based on detection of broad emission lines and high-ionization emission lines such as He II and N V (Laporte et al. 2017; Harikane et al. 2022a).

The James Webb Space Telescope (JWST) has just provided its first infrared images in 2022 July. The 6.5 m space observatory is expected to be a game changer in the field of extragalactic observations. Numerous papers have claimed the first detection of ultra high-redshift galaxies at $z \gtrsim 10$, waiting for spectroscopic confirmation (e.g., Adams et al. 2023; Castellano et al. 2022; Donnan et al. 2023; Finkelstein et al. 2022a, 2022b; Harikane et al. 2022b; Naidu et al. 2022). Likewise, the superb sensitivity of JWST may also enable us to witness rapidly accreting seed BHs far beyond the current samples of high-redshift AGNs. (e.g., Natarajan et al. 2017; Valiante et al. 2018; Goulding & Greene 2022; Inayoshi et al. 2022b).[8]

We here report a candidate low-luminosity AGN at $z = 5$, slightly after the end of cosmic reionization. This candidate was selected with the first imaging data set of the Cosmic Evolution Early Release Science Survey (CEERS; Finkelstein et al. 2017), one of the 13 JWST Cycle 1 Early Release Science (ERS) programs. In Section 2, we present our imaging data set and parent sample of $z > 4$ LBGs. Section 3 presents our discovery of a promising AGN candidate and its photometric properties. Our spectral fitting analysis and constraint on the $z = 5$ AGN luminosity function is discussed in Section 4, followed by our future prospects in Section 5. All magnitudes quoted in this Letter are in the AB system and are corrected for Galactic extinction (Schlafly & Finkbeiner 2011). ΛCDM cosmology is adopted with $H_0 = 70$ km s^{-1} Mpc^{-1}, $\Omega_M = 0.3$, and $\Omega_\Lambda = 0.7$, leading to a scale of 6.28 kpc arcsec^{-1} at $z = 5$.

2. Candidate Selection

2.1. Sample

The parent sample of our selection is a catalog of $z = 2$–9 LBGs compiled by Bouwens et al. (2021). This sample was obtained from multiple imaging surveys of the HST. The CANDELS Extended Groth Strip (EGS) field is covered by the JWST CEERS program. A multiwavelength (0.4–8 μm) source catalog down to HST/WFC3 F160W magnitude 26.62 was made available by Stefanon et al. (2017).

This LBG catalog with multiwavelength photometry is ideal to characterize the near-infrared (NIR) spectral energy distribution (SED) of $z > 4$ LBGs and search for low-luminosity AGNs. We thus initiated our low-luminosity AGN survey by finding JWST counterparts of those known LBGs.

2.2. Data Reduction

The data we analyze in this Letter are the first CEERS images taken by the Near Infrared Camera (NIRCam; Rieke et al. 2005) on 2022 June 20. The CEERS survey employs seven filters of NIRCam (F115W, F150W, F200W, F277W, F356W, F410M, and F444W) that cover 1–5 μm. At the time of writing this Letter, the full-band coverage of NIRCam is four pointings (CEERS1, CEERS2, CEERS3, and CEERS6) of the NIRCam's $2'.2 \times 4'.4$ fields of view, or 34.5 arcmin^2. The total exposure times for each filter is about 2835 s, while F115W has twice longer exposure times. More details of the

survey design and the Epoch 1 NIRCam observations of the CEERS program are presented by the ERS team (Bagley et al. 2022).

We downloaded the archival Stage 2 data products from the STScI MAST Portal.[9] The Stage 2 images were processed with the JWST pipeline version 1.5.3 with the pipeline mapping file jwst_0942.pmap except for F410M and F444W. For those two reddest filters multiple pmap files are used (jwst_0877.pmap and jwst_0878.pmap for F410M; jwst_0877.pmap, jwst_0878.pmap, and jwst_0881.pmap for F444W), depending on the fields. The Stage 2 images were postprocessed as follows. It is known that the version 1.5.3 pipeline has an issue in the imaging background subtraction.[10] We first subtracted the global background with photutils's Background2D function. There is a clear horizontal and vertical pattern in the current NIRCam images due to detector readnoise. The so-called $1/f$ noise was removed with the script provided by the CEERS team.[11]

Those postprocessed Stage 2 frames were then stacked by the JWST Stage 3 pipeline. During the Resample step, we decreased the final pixel sampling size by a factor of 2 with the drizzle algorithm. This procedure yields the final pixel sizes of $0''.0156$ per pixel in Short Wavelength filters (F115W, F150W, and F200W) and $0''.0315$ per pixel in Long Wavelength filters (F277W, F356W, F410M, and F444W). The Stage 3 images were aligned to match the coordinates of unsaturated GAIA sources inside each field of view based on its DR3 source catalog (Gaia Collaboration et al. 2016). Finally, we referred to the postflight flux calibration files that contain conversion factors from pixel signals per second to mega Jansky per steradian unit (jwst_nircam_photom_0101.fits for module A, and jwst_nircam_photom_0104.fits for module B). This process was needed to correct the preflight measurements applied in the original images. The difference of the pre- and postflight photometric reference files is significant, as is also discussed in Adams et al. (2023). With the updated calibration, the F410M and F444W flux densities (in mega Jansky per steradian unit) decrease by 10%–20% in the two NIRCam detector modules.

We also examined the consistency of photometry between images of JWST/NIRCam and HST/WFC3 that cover similar wavelength ranges. We performed aperture photometry for isolated bright stars inside the current footprints of CEERS. For HST, we use the WFC3 images processed by the CEERS team.[12] We use apertures with $4''.5$ diameter for both NIRCam and WFC3 images for this test. This aperture size is large enough to accumulate the entire light of a star. As a result, we found that the NIRCam F115W magnitudes offset from the HST/WFC3 F125W magnitudes by -0.05 mag. Likewise, the NIRCam F150W magnitudes have ~ -0.20 to -0.15 mag offsets with respect to the WFC3 F140W and F160W magnitudes. Since the two WFC3 filters straddle the transmission curve of NIRCam F150W, this offset cannot be explained by stellar SEDs. Therefore, we added $+0.05$ mag to our photometry for F115W and $+0.15$ mag for F150W. The amount of possible offsets for the other filters (F200W, F277W, F356W, F410M, and F444M) is uncertain at this stage, because there are no HST filters that match with those

---

[8] Ono et al. (2022) report an AGN candidate at $z \sim 12$ (GL_z12_1) based on their morphology analysis of $z \simeq 9$–17 galaxy candidates.

[9] https://archive.stsci.edu/

[10] https://github.com/spacetelescope/jwst/issues/6920

[11] https://ceers.github.io/releases.html#sdr1

[12] CEERS HST data release v1: https://ceers.github.io/releases.html#hdr1

NIRCam filters. The absolute flux calibration that we use has 20% uncertainty in all filters, which is consistent with our offset measurements for F115W and F150W. We thus added 0.2 mag to the uncertainty of photometry for all NIRCam filters, which dominates the error budget for our LBGs. Further analyses of the ongoing JWST calibration programs are needed to better perform photometry with NIRCam.

2.3. Visual Selection of Point Sources

The NIRCam images of $z > 4$ LBGs in the CEERS field were visually inspected by one of the authors (M. Onoue). We focus on compact sources in this study, because we are interested in sources dominated by the central BH radiation. We note that the UV luminosity function at the faint end (rest-frame UV magnitude $m_{UV} \gtrsim 24$ mag, or $M_{UV} \gtrsim -22$ mag in the absolute frame) is dominated by star-forming galaxies (Bowler et al. 2021; Adams et al. 2022; Harikane et al. 2022a). In this sense, our morphology selection is only sensitive to a subsample of AGN populations at high redshift, the host galaxies of which are outshined by the central AGNs or have compact morphology.

The visual inspection of the known $z > 4$ LBGs returned approximately 20 compact sources without any noticeable extended components or interacting sources. We ran SExtractor (Bertin & Arnouts 1996) for those compact sources to perform initial photometry. We require that the difference between the SExtractor's MAG_AUTO and aperture magnitudes (MAG_APER) with $0\farcs33$ diameter ($\times 5$ image FWHM) be less than 0.3 mag in the F200W images. Eight objects satisfy this criterion.

We hereafter present one of the compact sources we found from the selection above, CEERS-AGN-z5-1, or EGSV-9176349491 in the original CANDELS catalog with the photometric redshift $z = 4.71$. This source is the only source among the eight that shows F115W − F356W > 0.5 mag (and F115W − F444W > 1.5 mag) based on MAG_AUTO. This unique color is reminiscent of an unobscured AGN, as we present later in this Letter. The NIRCam coordinate of CEERS-AGN-z5-1 is (R.A., decl.) = (14:19:17.629, +52:49:49.04). We crossmatch this source with the CANDELS catalog (Stefanon et al. 2017) to compile their optical-to-NIR photometric information.

3. Results

3.1. A Candidate AGN at z = 5

CEERS-AGN-z5-1 shows a remarkably red NIRCam color among the selected compact LBGs, based on our initial SExtractor photometry. The unique photometric color was later confirmed by our additional photometry with a two-dimensional image modeling tool Galight (Ding et al. 2020, 2021), which we report in Table 1. The photometry with Galight assumes that the central source is a combination of point-spread function (PSF) and a two-dimensional Sérsic profile. The PSF models applied in each filter are based on a library of point-source profiles sampled from the CEERS images. More details on the Galight analysis with JWST images are presented in Ding et al. (2022). In this Letter, we use the total magnitudes to characterize the SED of CEERS-AGN-z5-1 in the following analysis. We found that the central pixels in the F115W image are dominated by the PSF, which indicates that the effective radius is $<0\farcs02$, or <0.13 kpc. This

Table 1
Optical-to-NIR Photometry of CEERS-AGN-z5-1 and the Companion Source

Filter	CEERS-AGN-z5-1	Companion
JWST/NIRCam F115W	26.6 ± 0.2	27.6 ± 0.2
JWST/NIRCam F150W	26.5 ± 0.2	27.4 ± 0.2
JWST/NIRCam F200W	26.3 ± 0.2	27.5 ± 0.2
JWST/NIRCam F277W	25.3 ± 0.2	28.9 ± 0.2
JWST/NIRCam F356W	25.8 ± 0.2	28.7 ± 0.2
JWST/NIRCam F410M	24.5 ± 0.2	...
JWST/NIRCam F444W	25.1 ± 0.2	...
CFHT/MegaCam u^*	>27.9	
CFHT/MegaCam g'	>28.5	
CFHT/MegaCam r'	>28.0	
CFHT/MegaCam i'	26.5 ± 0.2	
CFHT/MegaCam z'	>26.8	
HST/ACS F606W	>28.2	
HST/ACS F814W	26.7 ± 0.2	
HST/WFC3 F105W	26.6 ± 0.2	
HST/WFC3 F125W	26.8 ± 0.2	
HST/WFC3 F140W	26.7 ± 0.2	
HST/WFC3 F160W	26.6 ± 0.2	
Spitzer/IRAC 3.6μm	>25.0	
Spitzer/IRAC 4.5μm	24.9 ± 0.3	

Note. The photometric errors for NIRCam filters are from the 20% uncertainty of the absolute flux calibration. The CFHT, HST/ACS, and Spitzer photometry is from the multiwavelength catalog of Stefanon et al. (2017). The HST/WFC3 magnitudes are updated based on our Galight photometry. 3σ upper limits are provided for filters with no detection. We note that our SExtractor MAG_AUTO photometry for CFHT i' band and HST/ACS F814W returns brighter magnitudes than reported here by ≈ 0.2–0.3 mag, and we get 2.9σ detection in CFHT z' band. Nevertheless, we use Stefanon et al.'s values to be consistent with other filters. This difference does not have a major effect on our SED fitting analysis in Section 4.1.

upper limit of the source size is well below the 1σ range of $z \sim 5$ LBGs at the rest-frame UV magnitude of -20.0 (0.3–1.0 kpc; Shibuya et al. 2015). The CFHT, HST, and Spitzer magnitudes available for this source are also reported in Table 1, while for HST/WFC3 filters we also applied Galight to update the photometry from the catalog. There is no X-ray counterpart in the Chandra catalog of Nandra et al. (2015) within a $5''$ search radius.

We note that there is a faint companion source visible in the NIRCam images (Figure 1). The NIRCam coordinate of this source is (R.A., decl.) = (14:19:17.628, +52:49:48.79), approximately $0\farcs23$ to the south of CEERS-AGN-z5-1. The 2D flux distribution of this companion is simultaneously fitted with the main source by Galight to deblend the two sources, as we report in Table 1. This companion is not identified in the reddest F410M and F444W filters. The possible blending of the companion source in these red filters is likely a minor issue, because the companion is ≈ 1 mag fainter than CEERS-AGN-z5-1 in the SW filters and the difference becomes larger with >2 mag for F277W and F356W.

Figure 1 shows the NIRCam cutout images and the optical-to-NIR SED of CEERS-AGN-z5-1. Thanks to the wealth of photometry available in the CEERS field, the rest-frame UV-to-optical SED of CEERS-AGN-z5-1 is clear. There is a strong Lyman break between CFHT r' and i' bands (and HST/ACS F814W). The observed continuum redward of Lyman break is red with F115W − F356W = 0.8 ± 0.3. Moreover, there is a clear color excess at 3 μm (F277W) and 4 μm (F410M, F444W, and
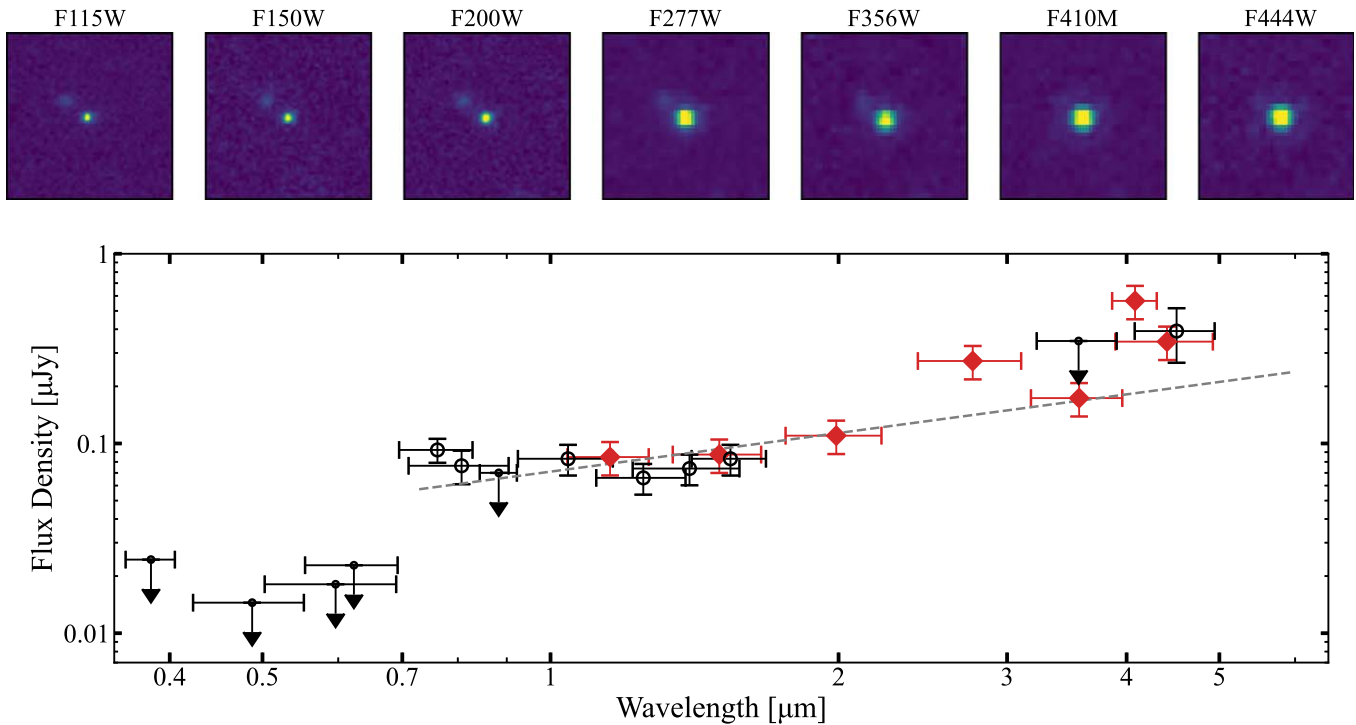
Figure 1. The $z = 5$ AGN candidate presented in this Letter, CEERS-AGN-z5-1. Top: the snapshot images of seven NIRCam filters employed in CEERS. The image size of each panel is $1''\!.5 \times 1''\!.5$. There is a companion source to the upper left from the central source. Bottom: the optical-to-NIR SED of CEERS-AGN-z5-1. The NIRCam flux densities based on model magnitudes are presented in red. CEERS-AGN-z5-1 has an entry in the CANDELS catalog of Stefanon et al. (2017). Here we show optical CFHT/MegaCam (u^*, g', r', i', and z'), HST/ACS (F606W and F814W) + WCS3 (F105W, F125W, F140W, and F160W), and Spitzer/IRAC (3.6 μm and 4.5 μm) in black. Three sigma upper-limit flux densities are shown for those with signal-to-noise ratios less than 3. Horizontal and vertical error bars correspond to the filter bandwidths and photometric errors, respectively. The gray dashed line shows our best-fit power-law continuum model, where the continuum slope index is $\alpha_\lambda = -1.32 \pm 0.30$.

IRAC 4.5 μm), while F356W traces the continuum in between. This excess matches with the redshifted Hβ+[O III] and Hα emission lines, respectively. The strong excess of F410M suggests that the Hα emission line is within the F410M coverage. Those photometric features suggest that CEERS-AGN-z5-1 is a $4.9 \lesssim z \lesssim 5.6$ source with emission lines so strong that they affect broadband/mediumband photometry, as we discuss in more detail later (Sections 3.3 and 4.1).

3.2. Continuum Properties

The broadband photometry of CEERS-AGN-z5-1 is well reproduced by a continuum model with a single power-law function, except for filters that cover strong emission, especially Hβ+[O III] and Hα. Our best-fit model based on photometry for F115W, F150W, and F200W filters suggests a power-law slope α_λ ($\equiv \mathrm{dln}F_\lambda/\mathrm{dln}\lambda$) of -1.32 ± 0.30, which is consistent with a typical value for type 1 quasars (e.g., Fan et al. 2001b; Vanden Berk et al. 2001, hereafter VB01). With five more filters from CFHT z' band and HST/WFC3 (F105W, F125W, F140W, and F160W), the slope gets slightly flatter with a larger error ($\alpha_\lambda = -1.25 \pm 0.76$). In what follows, we adopt the former model with NIRCam only, which is presented in the bottom panel of Figure 1 (dashed line). Note that the different choice of the spectral index causes only <7% of the difference in the estimated continuum flux density at rest-frame 3000 and 5100 Å.

Adopting the fitted spectral index, we estimate the absolute magnitude at rest-frame 1450 Å as $M_{1450} = -19.5 \pm 0.3$ mag at $z = 5$. The monochromatic luminosities at rest-frame 3000 Å and 5100 Å are $\lambda L_{3000} = 4.6 \pm 0.5 \times 10^{43}$ erg s^{-1} and

$\lambda L_{5100} = 3.9 \pm 0.4 \times 10^{43}$ erg s^{-1}, respectively. The rest-frame UV brightness of CEERS-AGN-z5-1 is more than three magnitudes fainter than those for spectroscopically confirmed $z \sim 5$ quasars from the moderately deep optical survey by Subaru/HSC (Niida et al. 2020). We estimate the bolometric luminosity by applying the bolometric correction for λL_{3000} (Richards et al. 2006),[13] which yields $L_{\rm bol} = 5.15 \times \lambda L_{3000} = 2.5 \pm 0.3 \times 10^{44}$ erg s^{-1}. The expected BH mass is $M_{\rm BH} = 2 \times 10^6\,M_\odot$ if we assume Eddington-limit accretion. The inferred bolometric luminosity becomes $L_{\rm bol} = 4.1 \pm 0.4 \times 10^{44}$ erg s^{-1} when we use the correction factor of 9.26 for λL_{5100} instead.

Figure 2 shows the BH mass–bolometric luminosity plane for AGNs at different redshift ranges. The inferred bolometric luminosity of CEERS-AGN-z5-1 is more than 2 dex smaller than those of the typical $z = 1$–2 Sloan Digital Sky Survey (SDSS) DR7 quasars with $L_{\rm bol} \simeq 10^{46.5}$ erg s^{-1} (Shen et al. 2011) and those of known $z \gtrsim 5$ quasars with virial BH masses available from Mg II (Willott et al. 2010; Trakhtenbrot et al. 2011; Matsuoka et al. 2019; Onoue et al. 2019; Kato et al. 2020). The luminosity of CEERS-AGN-z5-1 is comparable to those for typical low-redshift ($z < 0.35$) broad-line AGNs (Liu et al. 2019). In Figure 2, we show that some $M_{\rm BH} \sim 10^6\,M_\odot$ BHs from Greene & Ho (2007) and Liu et al. (2018) have comparable luminosities to CEERS-AGN-z5-1. An even less

---

[13] The bolometric luminosities of Richards et al.'s (2006) sample are $L_{\rm bol} > 10^{45}$ erg s^{-1}, approximately a half dex higher than that of CEERS-AGN-z5-1. The luminosity dependence of bolometric correction is discussed in, for example, Netzer (2019). With their prescription, the bolometric correction factors become twice larger for CEERS-AGN-z5-1.
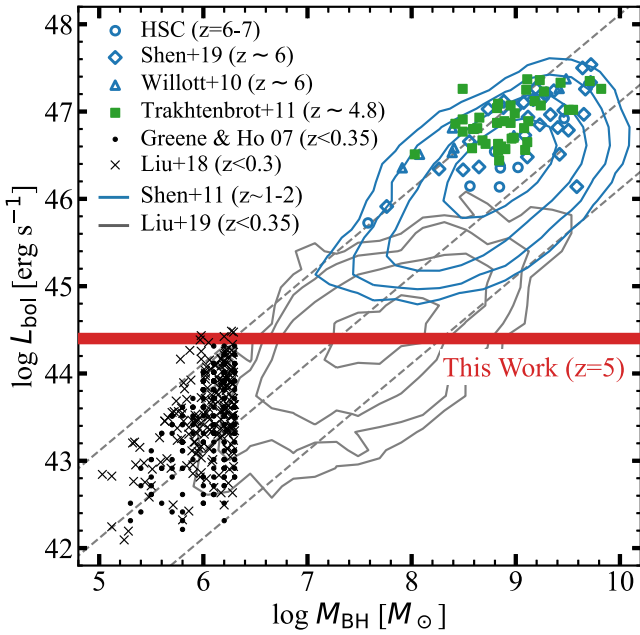
Figure 2. The BH mass–bolometric luminosity plane. The bolometric luminosity of CEERS-AGN-z5-1 ($L_{\rm bol} = 2.5 \times 10^{44}$ erg s^{-1}; red line) is estimated from its 3000 Å monochromatic luminosity. The virial BH masses of broad-line AGNs at various redshift ranges are also shown for comparison. Blue symbols are $z > 6$ quasars from Subaru/HSC (circle; Matsuoka et al. 2019; Onoue et al. 2019; Kato et al. 2020), SDSS (diamond; Shen et al. 2019), and CFHQS (triangle; Willott et al. 2010). Green squares show $z \sim 4.8$ quasars from Trakhtenbrot et al. (2011). The blue contour is the normalized distribution of SDSS DR7 quasars with a logarithm step of 0.5 dex. (Shen et al. 2011). The BH masses from the literature above are estimated based on Mg II λ2798. The gray contour shows the normalized distribution of low-redshift ($z \lesssim 0.35$) broad-line AGNs (Liu et al. 2019) with the same step as for Shen et al.'s $z \sim 1$–2 distribution. Black symbols are the individual low-redshift AGNs with estimated BH masses $M_{\rm BH} \lesssim 10^{6.3} M_\odot$ from Greene & Ho (2007; dot), and Liu et al. (2018; cross). Those low-redshift samples use Balmer lines to estimate BH masses. Clearly, CEERS-AGN-z5-1 has the typical luminosity of the $z < 0.35$ AGNs with $M_{\rm BH} \gtrsim 10^6 M_\odot$. The three diagonal lines indicate 100%, 10%, and 1% Eddington luminosity from top left to bottom right.

massive BH can power this source if rapid super-Eddington accretion is achieved. The necessity of such intermittent super-Eddington phases has been recently argued in theoretical predictions of early BH assembly (Hu et al. 2022; Inayoshi et al. 2022a; Shi et al. 2023). On the other hand, the same luminosity can also be achieved by a sub-Eddington BH with $M_{\rm BH} \simeq 10^{7-8} M_\odot$, as long as the nuclear accretion disk settles down to a radiatively efficient state ($L_{\rm bol}/L_{\rm Edd} \gtrsim 0.01$; see Yuan & Narayan 2014). Spectroscopic follow-up observations of broad Balmer lines or other virial BH mass tracers such as Mg II λ2798 are necessary to robustly estimate the BH mass of CEERS-AGN-z5-1.

3.3. Broadband/Mediumband Excess

We now quantify the broadband/mediumband excess due to Hβ+[O III] and Hα. Here we consider the NIRCam photometry of F277W, F410M, and F444W, and use our continuum model with a single power-law index $\alpha_\lambda = -1.32$ (Section 3.2). The observed F277W magnitude is 0.7 mag brighter than that expected from the continuum flux at F277W, which is significantly larger than the photometric error (0.2 mag). This excess is consistent with a luminosity for the Hβ+[O III] lines of $L_{\rm H\beta+[O\ III]} = 10^{43.0}$ erg s^{-1} and rest-frame equivalent width

EW$_{\rm H\beta+[O\ III]} = 1100$ Å. The Hα excess in F410M and F444W, 1.2 and 0.6 mag, respectively, is explained by a strong Hα emission with line luminosity $L_{\rm H\alpha} = 10^{42.9}$ erg s^{-1} and rest-frame equivalent width EW$_{\rm H\alpha} = 1600$ Å. In addition, assuming the relation of $L_{\rm H\alpha} = 3.1 L_{\rm H\beta}$ expected for Case B's recombination (e.g., Greene & Ho 2005), we infer the [O III] luminosity as $L_{\rm [O\ III]} \simeq 10^{42.9}$ erg s^{-1}. Note that these measurements slightly increase by 5% and 1% for Hβ+[O III] and Hα, respectively, when the second continuum model for $\alpha_\lambda = -1.27$ is used.

The two equivalent widths for Hβ+[O III] and Hα are extremely large as an AGN. The composite spectrum of low-redshift quasars of VB01 shows EW$_{\rm H\beta+[O\ III]} \simeq 63$ Å and EW$_{\rm H\alpha} \simeq 195$ Å. The brightest type 2 quasars in the local universe show equivalently strong [O III] line emission (both in terms of luminosity and equivalent width; e.g., Zakamska et al. 2003; Kong & Ho 2018), while their bolometric luminosity estimated from the extinction-corrected [O III] luminosity $L_{\rm bol} \sim 10^{47}$ erg s^{-1} is $\gtrsim$100 times higher than that of CEERS-AGN-z5-1 (Heckman et al. 2004). We also note that the estimated Hα luminosity of CEERS-AGN-z5-1 is 5 times higher than expected from the empirical relation between the Hα luminosity and the 5100 Å luminosity for low-redshift broad-line AGNs (Greene & Ho 2005, their Equation (1)).

Alternatively, strong Balmer emission lines can also be produced from star-forming galaxies. Such high values of EW$_{\rm H\alpha} \simeq 1000$ Å have been reported in $z > 6$ star-forming galaxies based on Spitzer and JWST (e.g., Endsley et al. 2021; Chen et al. 2023; Stefanon et al. 2022). However, those galaxies show a significantly steeper continuum slopes ($\alpha_\lambda \simeq -2.0$), compared to that of CEERS-AGN-z5-1. We will discuss the possible contribution of star-forming galaxies to the SED of CEERS-AGN-z5-1 in Section 4.1.

4. Discussion

4.1. SED Fitting

The available photometry of CEERS-AGN-z5-1 continuously covers the SED from Lyα to Hα. We here present our SED fitting analysis with templates of metal-poor galaxies, low-redshift quasars, and super-Eddington accreting BHs. The redshift range is limited to $4.0 \leqslant z \leqslant 6.0$ (with steps of 0.01), which is wide enough to cover the redshifted Hα emission with F410M. Intergalactic medium absorption is taken into account with the prescription of Madau (1995).

4.1.1. Metal-poor Galaxies

First, we attempt to reproduce the observed photometric SED with galaxy templates. We here adopt the galaxy SED models from Inoue (2011), where nebular emission lines are included for various metallicities of $Z = 0.02\ (Z_\odot)$, 0.008, 0.004, 0.0004, 10^{-5}, 10^{-7}, and 0.0 (no metals). The stellar mass spectrum is calculated by assuming a Salpeter initial mass function (IMF) with 1–100 $M_\odot$. We use models of constant star formation history with ages of 10, 100, and 500 Myr, while we test galaxy models with extremely young ages ($<$10 Myr) later in Section 4.1.4. We take into account dust attenuation by extinction laws of the Small Magellanic Cloud (SMC; Prevot et al. 1984) and of starburst galaxies (Calzetti et al. 2000).

Figure 3(a) shows our best-fit model at $z = 4.93$ (chi-square $\chi^2 = 27$) with a metallicity $Z = 0.004$, stellar age 500 Myr, star formation rate (SFR) 3.6 $M_\odot$ yr^{-1}, and color excess $E(B - V) = 0.10$ mag with the Calzetti extinction law. This
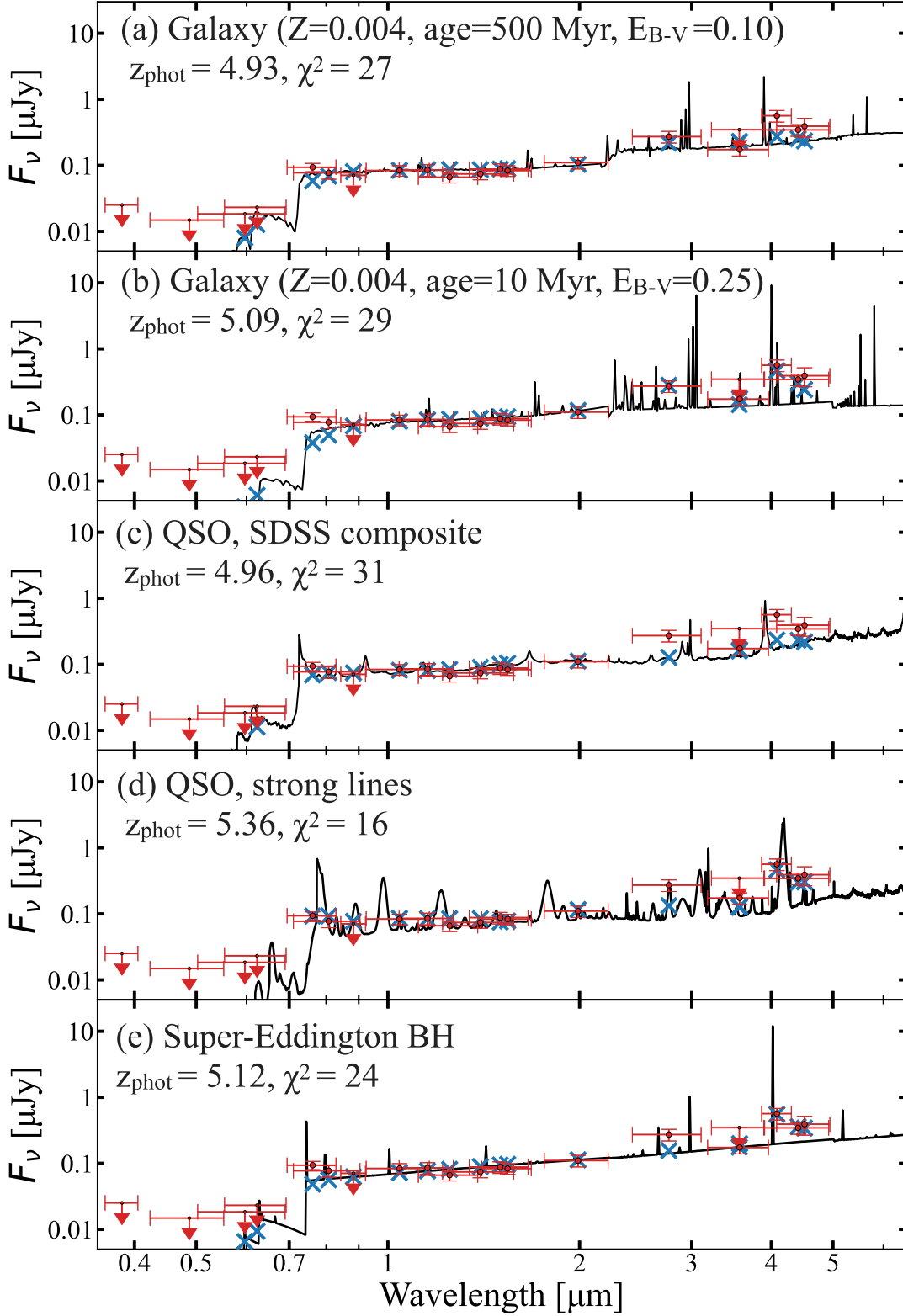
Figure 3. The results of our SED fitting. In each panel, we show the best-fit model of galaxies or AGNs with a black line. The photometric redshift and the chi-square of the best-fit model are shown at the upper left of each panel. The observed photometry is shown in red dots and the filter-convolved magnitudes of the best-fit models in blue crosses. (a) The best-fit galaxy template from Inoue's (2011) galaxy models. This model is a metal-poor ($Z = 0.004$) galaxy at $z = 4.93$ with a stellar age of 500 Myr, including dust attenuation of $E(B - V) = 0.1$ mag with the Calzetti law. (b) The best-fit galaxy model when the stellar age is fixed to 10 Myr. This model is also a $Z = 0.004$ galaxy with photometric redshift $z = 5.09$. Heavier dust attenuation ($E(B - V) = 0.25$ mag) by the Calzetti law is required to trace the continuum. (c) The low-redshift composite quasar spectrum of Vanden Berk et al. (2001) scaled to match the photometry of CEERS-AGN-z5-1. (d) The same low-redshift composite spectrum with emission lines added to match Hα. See the text for the details of the procedure. (e) The SED model of an accreting super-Eddington BH (Inayoshi et al. 2022a). The scale of the best-fit model corresponds to the central BH mass of $M_{BH} = 10^{6.3} \, M_\odot$.

model can well explain the observed continuum owing to modest dust attenuation. However, the model hardly reproduces the observed flux densities of the filters affected by Hβ+[O III] (F277W) and Hα emission lines (F410M, F444W, and IRAC 4.5 μm), while they are slightly raised by active starbursts.

We also show in Figure 3(b) the best-fit case when the age is fixed to 10 Myr ($Z = 0.004$ and SFR $= 27$ $M_\odot$ yr^{-1}). This model can better explain the photometric excess by Hβ+[O III] and Hα emission lines than the previous galaxy model with 500 Myr age. However, this model requires heavier extinction of $E(B - V) = 0.25$ mag with the Calzetti law, which leads to a poorer fit around Lyα. Nonetheless, the goodness of fit becomes just slightly worse ($\Delta\chi^2 = 2$).

For those galaxy models, it is worth noting the dependence of the fitting goodness on the choice of dust extinction/attenuation laws. Since the SMC law has a steeper slope than the Calzetti law in the rest-frame UV wavelengths, it gets more difficult to match the galaxy models to the observed SED, which has a flat slope around Lyα. As a result, the best-fit galaxy model with the SMC law is the same as what we show in Figure 3(a) (i.e., 500 Myr age with a milder extinction of $E(B - V) = 0.05$ mag), but returns a poorer fit ($\Delta\chi^2 = 7$). The disagreement between the observations and the models becomes more serious when only the galaxy models with 10 Myr age are considered, because the SEDs of young galaxies need to be more strongly obscured. One has to consider $E(B - V) \simeq 0.30$ mag to fit the young galaxy model to the rest-optical spectrum with the SMC law, which yields a substantially worse fit than the model presented in Figure 3(b) ($\Delta\chi^2 \simeq 50$) owing to the mismatch at the rest-frame UV wavelengths.

4.1.2. AGNs with Strong Emission Lines

Next, we test the composite spectrum of low-redshift quasars compiled by VB01. This composite spectrum from the SDSS covers the rest-wavelength 800–8555 Å and includes 80 resolved emission-line features in the spectrum. The continuum index measured at rest-frame 1300–5000 Å is $\alpha_\lambda = -1.56$. Figure 3(c) shows the scaled spectrum at $z = 4.96$ matched to CEERS-AGN-z5-1 ($\chi^2 = 31$). This model agrees with the observed continuum of CEERS-AGN-z5-1 well; however, the broadband/mediumband excess due to Hβ+[O III] and Hα is not sufficiently reproduced (Section 3.3).

The composite spectrum of VB01 is constructed based on luminous quasars, unlike CEERS-AGN-z5-1. It is observationally known that the strength of quasar emission lines increases as the continuum luminosity decreases (Baldwin 1977). To mimic the so-called Baldwin effect, we increase the strength of *all* the emission lines listed in Table 2 of VB01, so that the relative flux ratio of each line is maintained.[14] We add those additional emission-line fluxes to the original spectrum assuming Gaussian profiles with the same line widths as those measured in VB01. This modified version of the VB01's quasar SED model is presented in Figure 3(d), in which case a better goodness of fit is achieved at $z = 5.36$ ($\chi^2 = 16$) than the original composite spectrum. The excess of Lyα and Hα is better reproduced than the original model in this case; however, the observed flux density at F277W is still twice as high than predicted from this third model.

---

[14] We do not increase the strength of the unresolved iron pseudocontinuum in the original spectrum.

4.1.3. Super-Eddington Accreting BHs

As an alternative scenario, we consider a more theory-based SED model for a super-Eddington accreting BH with $M_{BH} \sim 10^6 M_\odot$ (Inayoshi et al. 2022b). The SED model is constructed by postprocess line transfer calculations with CLOUDY (C17; Ferland et al. 2017), which is applied to the results of radiation hydrodynamical simulations of a seed BH rapidly growing in the protogalactic nucleus (Inayoshi et al. 2022a). In this model, several prominent lines are powered by the central BH fed via a dense accretion disk at super-Eddington rates. Among them, strong Hα line emission with a rest-frame EW$_{H\alpha} \simeq 1300$ Å is so prominent that the line flux affects the broadband colors significantly, just like we observe in CEERS-AGN-z5-1.

Figure 3(e) shows the best-fit model of a super-Eddington accreting BH ($\chi^2 = 24$) scaled to $z = 5.12$. This model explains the continuum flux densities and the broadband/mediumband excess in F410M, F444W, and IRAC 4.5 μm, owing to the strong Hα emission powered by the fast-growing BH. The overall flux normalization of the best-fit case is only 1.4 times higher compared to the original SED model, suggesting that the predicted line information (e.g., low-ionization emission lines of O I $\lambda\lambda1304$ and C II] $\lambda2326$) is still valid and can be tested by follow-up spectroscopic observations of CEERS-AGN-z5-1. This model yields a slightly larger χ^2 value compared to the quasar model with enhanced emission lines (Figure 3(c)), but we note that the SED model for a super-Eddington BH does not include the broad-line components that could be produced in the inner region but are unresolved in their simulations.

4.1.4. Caveats

Based on our SED fitting analysis, we propose that there are two plausible solutions to explain the observed SED for CEERS-AGN-z5-1: an unobscured AGN with strong broad-line emission (Figure 3(d)) and a low-mass super-Eddington accreting BH (Figure 3(e)). Those two models well reproduce the continuum shape and the Hα excess, both of which originate from the nuclear region of the AGN. On the other hand, let us recall that neither of the two models can explain the broadband excess of F277W, which is likely dominated by [O III] emission. Since this forbidden line is not efficiently produced from the dense gas at the nuclear region, we hypothesize that the F277W excess is at least partly attributed to the ionized gas at the host-galaxy scale. For example, a metal-poor galaxy with age $\simeq 10$ Myr can produce strong [O III] emission required to explain the observed magnitude of F277W, when SFR $\simeq 30 M_\odot$ yr^{-1} (see Figure 3(b)). We note that this order estimate does not consider the contribution of the host to other filters.

Alternatively, a top-heavy stellar IMF expected in metal-poor environments can also be another solution to produce strong [O III] emission lines from galaxies, which is not taken into account in the galaxy models we use in this Letter. It is also possible that the nebular gas is oxygen-rich in low metallicity relative to the solar value, which enhances the strength of [O III] emission without changing the value of metallicity. The detailed modeling of the additional galaxy SED is left for future investigation.

One may also consider a young galaxy with age $\lesssim 10$ Myr without AGN contribution, as is discussed in Section 4.1.1 and also in the literature (e.g., Inoue 2011; Wilkins et al. 2020; Tang et al. 2021). Indeed, observations with HST, Spitzer, and

JWST have suggested that the photometric SEDs of some $z \gtrsim 6$ galaxies are consistent with those of young stellar populations down to ∼3 Myr ages (e.g., Tamura et al. 2019; Endsley et al. 2021; Chen et al. 2023; Endsley et al. 2022). We additionally conduct the SED fitting analysis extending the stellar age down to 1 Myr with delayed star formation history and find that a model of a metal-poor galaxy with a metallicity $Z = 0.004$, stellar age 1.4 Myr, and SFR $\simeq 400 M_{\odot}$ yr^{-1} yields the smallest value of $\chi^2 = 21$ among the galaxy models. This model specifically needs dust extinction following the Calzetti's law with color excess $E(B - V) = 0.22$ mag. This level of dust attenuation produces the infrared luminosity of $\sim 10^{11.3} L_{\odot}$, which is converted to the dust mass of $\sim 10^7 M_{\odot}$ by assuming a dust temperature of $T_d = 40$ K (see Equation (5) of Inoue et al. 2020). However, this amount of dust is hardly produced by the ongoing active star formation within ≈1 Myr unless a preexisting stellar population leaves dust grains, and their older (≫1 Myr) stellar components are hidden in the observed SED (e.g., Tamura et al. 2019).

4.2. z = 5 AGN Luminosity Function (LF)

The discovery of the promising candidate of a high-redshift AGN was unexpected from the first CEERS data set. To quantify the serendipity, we discuss the number density of $z \sim 5$ AGNs based on CEERS-AGN-z5-1. We caution that we can only provide a lower bound of the AGN luminosity function with this work especially because we do not consider AGNs embedded in their host galaxies with extended morphology. Such a population would be common for faint AGNs at UV magnitudes dominated by star-forming galaxies.

Figure 4 shows our estimate of the $z \sim 5$ AGN luminosity function. We calculate the binned number density as $\Phi = 1.03 \times 10^{-5}$ Mpc^{-3} mag^{-1} at $M_{1450} = -19.5$ mag (red), where we adopt the survey area of 34.5 arcmin^2 and set $z = 5.15$ and its interval of $\Delta z = \pm 0.5$ to calculate the cosmic volume. For comparison, we overlay the binned quasar luminosity functions derived from Subaru/HSC+SDSS (Niida et al. 2020) and CFHT Legacy Survey (McGreer et al. 2018). We also show the $z = 4.5$ X-ray-detected AGN luminosity function in the CANDELS fields (including EGS), which go down to $M_{1450} = -18.5$ mag (Giallongo et al. 2019).[15] In Figure 4, we take the face values of their $z = 4.5$ luminosity function without correcting for redshift evolution. The abundance of the faintest AGNs at $M_{1450} = -19.5$ mag is substantially higher than that expected from extrapolation of the HSC+SDSS quasar LFs (short dashed; Niida et al. 2020), while the extrapolation of their double power-law LF is still consistent with our data point within the Poisson error of one object. Intriguingly, our binned luminosity function is rather consistent with those of Chandra-detected (0.5–2 keV) X-ray sources from Giallongo et al. (2019), while we caution that neither of them are spectroscopically confirmed.

5. Future Prospects

Spectroscopic follow-up observations are the key to confirming the redshift and the nature of CEERS-AGN-z5-1, and also our estimate of the $z = 5$ AGN luminosity function at the very faint end, where galaxies are dominant against AGNs in number (Figure 4). Those observations will also help to test
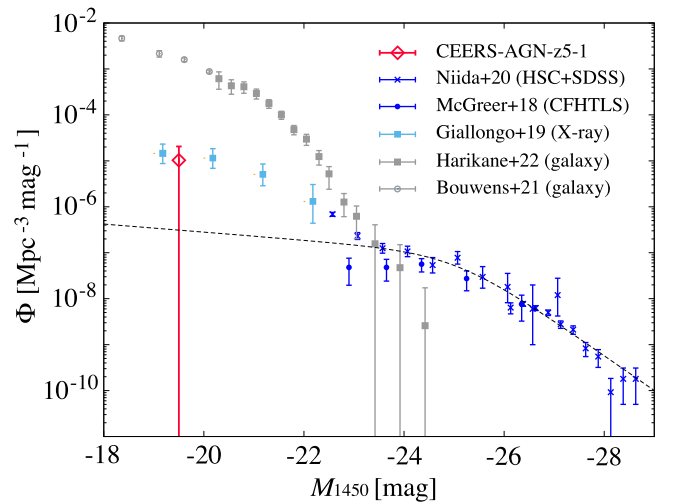

Figure 4. The $z \sim 5$ UV luminosity function of AGNs. Our constraint from CEERS-AGN-z5-1 is shown in red. The quasar luminosity function data obtained from different surveys are shown: the rest-UV-selected quasars combining Subaru HSC and SDSS (Niida et al. 2020, cross) and CFHTLS (McGreer et al. 2018, dot) in blue. The abundance of AGNs at $M_{1450} = -19.5$ mag is significantly higher than the extrapolation of the rest-UV-selected quasar LF (dashed line), while within the Poisson error from one object. Our data point is consistent with the AGN luminosity function from the X-ray-detected AGN candidates in the CANDELS field (Giallongo et al. 2019), which are shown in cyan. Shown in gray are the UV luminosity function of galaxies from Bouwens et al. (2021; circle) and Harikane et al. (2022a; square).

the extreme emission-line properties that we discuss in Sections 3.3 and 4.1. Specifically, detection of broad-line emission will enable us to perform a virial BH mass estimate via Balmer lines or other mass tracers such as Mg II, from which one can constrain the mass distribution of seed BHs in the earlier epochs of the universe (Toyouchi et al. 2022; see also Greene et al. 2020; Inayoshi et al. 2020).

Our initial result based on the first observations of the CEERS program indicates that deep NIR imaging observations of JWST are capable of determining the high-redshift AGN luminosity function at the very faint end. More complete and sophisticated AGN selection criteria are required to better constrain the underlying AGN population. Ongoing and upcoming wide-field surveys with JWST such as COSMOS Web and JADES programs can also be used to perform wider and deeper surveys of high-redshift AGNs.

ORCID iDs

Masafusa Onoue ⬤ https://orcid.org/0000-0003-2984-6803
Kohei Inayoshi ⬤ https://orcid.org/0000-0001-9840-4959
Xuheng Ding ⬤ https://orcid.org/0000-0001-8917-2148
Wenxiu Li ⬤ https://orcid.org/0000-0002-1044-4081
Zhengrong Li ⬤ https://orcid.org/0000-0002-8502-7573
Juan Molina ⬤ https://orcid.org/0000-0002-8136-8127
Akio K. Inoue ⬤ https://orcid.org/0000-0002-7779-8677
Linhua Jiang ⬤ https://orcid.org/0000-0003-4176-6486
Luis C. Ho ⬤ https://orcid.org/0000-0001-6947-5846

References

Adams, N. J., Bowler, R. A. A., Jarvis, M. J., Varadaraj, R. G., & Häußler, B. 2022, arXiv:2207.09342
Adams, N. J., Conselice, C. J., Ferreira, L., et al. 2023, MNRAS, 518, 4755
Astropy Collaboration, Robitaille, T. P., Tollerud, E. J., et al. 2013, A&A, 558, A33
Bagley, M. B., Finkelstein, S. L., Koekemoer, A. M., et al. 2022, arXiv:2211.02495
Baldwin, J. A. 1977, ApJ, 214, 679
Banados, E., Venemans, B. P., Mazzucchelli, C., et al. 2018, Natur, 553, 473
Bertin, E., & Arnouts, S. 1996, A&AS, 117, 393
Bouwens, R. J., Oesch, P. A., Stefanon, M., et al. 2021, AJ, 162, 47
Bowler, R. A. A., Adams, N. J., Jarvis, M. J., & Häußler, B. 2021, MNRAS, 502, 662
Bradley, L., Sipőcz, B., Robitaille, T., et al. 2022, astropy/photutils:, 1.4.0, Zenodo:10.5281/zenodo.6385735
Calzetti, D., Armus, L., Bohlin, R. C., et al. 2000, ApJ, 533, 682
Castellano, M., Fontana, A., Treu, T., et al. 2022, ApJL, 938, L15
Chen, Z., Stark, D. P., Endsley, R., et al. 2023, MNRAS, 518, 560
Ding, X., Birrer, S., Treu, T., & Silverman, J. D. 2021, arXiv:2111.08721
Ding, X., Silverman, J. D., & Onoue, M. 2022, ApJ, 939, L28
Ding, X., Silverman, J., Treu, T., et al. 2020, ApJ, 888, 37
Donnan, C. T., McLeod, D. J., Dunlop, J. S., et al. 2023, MNRAS, 518, 6011
Endsley, R., Stark, D. P., Chevallard, J., & Charlot, S. 2021, MNRAS, 500, 5229
Endsley, R., Stark, D. P., Whitler, L., et al. 2022, arXiv:2208.14999
Fan, X., Narayanan, V. K., Lupton, R. H., et al. 2001a, AJ, 122, 2833
Fan, X., Strauss, M. A., Richards, G. T., et al. 2001b, AJ, 121, 31
Ferland, G. J., Chatzikos, M., Guzmán, F., et al. 2017, RMxAA, 53, 385
Finkelstein, S. L., & Bagley, M. B. 2022, ApJ, 938, 25
Finkelstein, S. L., Bagley, M. B., Arrabal Haro, P., et al. 2022a, ApJL, 940, 55
Finkelstein, S. L., Bagley, M. B., Ferguson, H. C., et al. 2022b, arXiv:2211.05792
Finkelstein, S. L., Dickinson, M., Ferguson, H. C., et al. 2017, The Cosmic Evolution Early Release Science (CEERS) Survey, JWST Proposal ID 1345. Cycle 0 Early Release Science
Fujimoto, S., Brammer, G. B., Watson, D., et al. 2022, Natur, 604, 261
Gaia Collaboration, Prusti, T., de Bruijne, J. H. J., et al. 2016, A&A, 595, A1
Giallongo, E., Grazian, A., Fiore, F., et al. 2019, ApJ, 884, 19
Goulding, A. D., & Greene, J. E. 2022, ApJL, 938, L9
Greene, J. E., & Ho, L. C. 2005, ApJ, 630, 122
Greene, J. E., & Ho, L. C. 2007, ApJ, 670, 92
Greene, J. E., Strader, J., & Ho, L. C. 2020, ARA&A, 58, 257
Harikane, Y., Ono, Y., Ouchi, M., et al. 2022a, ApJS, 259, 20
Harikane, Y., Ouchi, M., Oguri, M., et al. 2022b, arXiv:2208.01612
Heckman, T. M., Kauffmann, G., Brinchmann, J., et al. 2004, ApJ, 613, 109
Hu, H., Inayoshi, K., Haiman, Z., et al. 2022, ApJ, 935, 140
Inayoshi, K., Nakatani, R., Toyouchi, D., et al. 2022a, ApJ, 927, 237
Inayoshi, K., Onoue, M., Sugahara, Y., Inoue, A. K., & Ho, L. C. 2022b, ApJL, 931, L25
Inayoshi, K., Visbal, E., & Haiman, Z. 2020, ARA&A, 58, 27
Inoue, A. K. 2011, MNRAS, 415, 2920
Inoue, A. K., Hashimoto, T., Chihara, H., & Koike, C. 2020, MNRAS, 495, 1577
Ishikawa, Y., Morishita, T., Stiavelli, M., et al. 2022, ApJ, 936, 167
Jiang, L., McGreer, I. D., Fan, X., et al. 2016, ApJ, 833, 222
Jiang, L., Ning, Y., Fan, X., et al. 2022, NatAs, 6, 850
Kato, N., Matsuoka, Y., Onoue, M., et al. 2020, PASJ, 72, 84
Kong, M., & Ho, L. C. 2018, ApJ, 859, 116
Laporte, N., Nakajima, K., Ellis, R. S., et al. 2017, ApJ, 851, 40
Li, W., Inayoshi, K., Onoue, M., & Toyouchi, D. 2022, arXiv:2210.02308
Liu, H.-Y., Liu, W.-J., Dong, X.-B., et al. 2019, ApJS, 243, 21
Liu, H.-Y., Yuan, W., Dong, X.-B., Zhou, H., & Liu, W.-J. 2018, ApJS, 235, 40
Madau, P. 1995, ApJ, 441, 18
Matsuoka, Y., Onoue, M., Kashikawa, N., et al. 2019, ApJL, 872, L2
Matsuoka, Y., Strauss, M. A., Kashikawa, N., et al. 2018, ApJ, 869, 150
McGreer, I. D., Fan, X., Jiang, L., & Cai, Z. 2018, AJ, 155, 131
Morishita, T., Stiavelli, M., Trenti, M., et al. 2020, ApJ, 904, 50
Naidu, R. P., Oesch, P. A., Setton, D. J., et al. 2022, arXiv:2208.02794
Nandra, K., Laird, E. S., Aird, J. A., et al. 2015, ApJS, 220, 10
Natarajan, P., Pacucci, F., Ferrara, A., et al. 2017, ApJ, 838, 117
Neeleman, M., Novak, M., Venemans, B. P., et al. 2021, ApJ, 911, 141
Netzer, H. 2019, MNRAS, 488, 5185
Niida, M., Nagao, T., Ikeda, H., et al. 2020, ApJ, 904, 89
Ono, Y., Harikane, Y., Ouchi, M., et al. 2022, arXiv:2208.13582
Ono, Y., Ouchi, M., Harikane, Y., et al. 2018, PASJ, 70, S10
Onoue, M., Kashikawa, N., Matsuoka, Y., et al. 2019, ApJ, 880, 77
Prevot, M. L., Lequeux, J., Maurice, E., Prevot, L., & Rocca-Volmerange, B. 1984, A&A, 132, 389
Richards, G. T., Lacy, M., Storrie-Lombardi, L. J., et al. 2006, ApJS, 166, 470
Rieke, M. J., Heaney, J. B., Burriesci, L. G., Kelly, D., & Horner, S. 2005, Proc. SPIE, 5904, 1
Schlafly, E. F., & Finkbeiner, D. P. 2011, ApJ, 737, 103
Shen, Y., Richards, G. T., Strauss, M. A., et al. 2011, ApJS, 194, 45
Shen, Y., Wu, J., Jiang, L., et al. 2019, ApJ, 873, 35
Shi, Y., Kremer, K., Grudić, M. Y., Gerling-Dunsmore, H. J., & Hopkins, P. F. 2023, MNRAS, 518, 3606
Shibuya, T., Ouchi, M., & Harikane, Y. 2015, ApJS, 219, 15
Stefanon, M., Bouwens, R. J., Illingworth, G. D., et al. 2022, ApJ, 935, 94
Stefanon, M., Yan, H., Mobasher, B., et al. 2017, ApJS, 229, 32
Stevans, M. L., Finkelstein, S. L., Wold, I., et al. 2018, ApJ, 863, 63
Tamura, Y., Mawatari, K., Hashimoto, T., et al. 2019, ApJ, 874, 27
Tang, M., Stark, D. P., Chevallard, J., et al. 2021, MNRAS, 503, 4105
Toyouchi, D., Inayoshi, K., Li, W., Haiman, Z., & Kuiper, R. 2022, MNRAS, 518, 1601
Trakhtenbrot, B., Netzer, H., Lira, P., & Shemmer, O. 2011, ApJ, 730, 7
Valiante, R., Schneider, R., Zappacosta, L., et al. 2018, MNRAS, 476, 407
Vanden Berk, D. E., Richards, G. T., Bauer, A., et al. 2001, AJ, 122, 549
Walter, F., Neeleman, M., Decarli, R., et al. 2022, ApJ, 927, 21
Wang, F., Yang, J., Fan, X., et al. 2021, ApJL, 907, L1
Wilkins, S. M., Lovell, C. C., Fairhurst, C., et al. 2020, MNRAS, 493, 6079
Willott, C. J., Albert, L., Arzoumanian, D., et al. 2010, AJ, 140, 546
Wu, X.-B., Wang, F., Fan, X., et al. 2015, Natur, 518, 512
Yang, J., Wang, F., Fan, X., et al. 2021, ApJ, 923, 262
Yuan, F., & Narayan, R. 2014, ARA&A, 52, 529
Zakamska, N. L., Strauss, M. A., Krolik, J. H., et al. 2003, AJ, 126, 2125